



Facile synthesis of highly dispersed and thermally stable copper-based nanoparticles supported on SBA-15 occluded with P123 surfactant for catalytic applications



Alexandru Chiriac^a, Brindusa Dragoi^{a,*}, Adrian Ungureanu^a, Carmen Ciotonea^{a,b,c}, Irina Mazilu^{a,b}, Sebastien Royer^{b,c,*}, Anne Sophie Mamede^c, Elisabetta Rombi^d, Italo Ferino^d, Emil Dumitriu^a

^a Faculty of Chemical Engineering and Environmental Protection, "Gheorghe Asachi" Technical University of Iasi, 73 Prof. Dr. Docent Dimitrie Mangeron Street, 700050 Iasi, Romania

^b CNRS UMR 7285, Université de Poitiers, IC2MP-TSA 51106-4, rue Michel Brunet, 86073 Poitiers Cedex 9, France

^c CNRS UMR 8181, Université de Lille 1, UCCS-Cité Scientifique, 59650 Villeneuve d'Ascq Cedex, France

^d Dipartimento di Scienze Chimiche, Università di Cagliari, Complesso Universitario Monserrato, S.S. 554 Bivio Sestu, 09042 Monserrato, Cagliari, Italy

ARTICLE INFO

Article history:

Received 11 January 2016

Revised 4 April 2016

Accepted 6 April 2016

Keywords:

Copper-based nanoparticles

P123 surfactant

SBA-15

Hydrogenation

Oxidation

ABSTRACT

Here, we show a strategy to control the dispersion, spatial distribution, and stabilization of copper-based nanoparticles on a micro-mesoporous silica support, as well as their impact on the catalytic activity. In this respect, SBA-15 with P123 occluded mesopores was used as host to load, by impregnation, copper-based nanoparticles, whose dispersion was similar to that of the homologous NPs prepared by precipitation on the SBA-15 with open mesoporosity, while the thermal stability was better. The oxide and reduced forms of the catalysts were rigorously characterized by ICP-OES, low- and high-angle XRD, N₂ physisorption, HRTEM/EDXS, TPR, in situ XRD, and in situ XPS. Due to their high practical impact, both the oxide and metallic forms of the copper-based NPs were evaluated for catalytic activity in CO oxidation and hydrogenation of cinnamaldehyde, respectively. It was shown that the high dispersion of copper-based NPs and the electron-deficient sites, such as M²⁺ with high affinity for the C=O bond, are responsible for the outstanding catalytic performance of the solids. The paper demonstrates that using a simple impregnation method and a functionalized SBA-15 support, high-performance materials can be obtained avoiding the use of precipitating agents and strict control of the synthesis conditions.

© 2016 Elsevier Inc. All rights reserved.

1. Introduction

Intense research efforts are being made nowadays on metal (oxide) nanoparticles (NPs) synthesis, due to the recognized advantages related to their size, shape, and dispersion, which make them useful in multiple areas, such as catalysis, chemical and biochemical sensors, drug delivery, energy storage, and pollution control [1–4]. Usually, their use as catalysts is accompanied by an intrinsic problem consisting of their low thermal stability, associated with the sintering phenomenon that occurs during catalytic reactions performed at temperatures above 400 °C (such as steam reforming, synthesis gas production, and partial oxidation reactions) and even during the activation or regeneration processes [5,6]. Therefore,

* Corresponding authors. Fax: +40 232 271311 (B. Dragoi); Fax: +33 320436561 (S. Royer).

E-mail addresses: bdragoi@tuiasi.ro (B. Dragoi), Sebastien.Royer@univ-lille1.fr (S. Royer).

there is a continuous interest in decreasing the size, while improving the spatial dispersion and thermal stability of NPs. For this purpose, many strategies have been proposed, such as trapping into organic agents (e.g., polymers, surfactants, microgels, amines [3], metal core coating within a mesoporous silica shell [6], deposition on inorganic supports (e.g., alumina, silica, titania, zirconia, carbon, aluminosilicates, and hydrotalcites) [7,8], deposition on organic-inorganic hybrid supports (e.g., amine-, thiol-, and carboxyl-modified silica support) [9–11], and addition of metal promoters [12–14]).

In 1998, SBA-15 mesoporous silica synthesis was reported using triblock copolymer (Pluronic P123, (poly(ethylene oxide)-block-poly(propylene oxide)-block-poly(ethylene oxide), EO₂₀PO₇₀EO₂₀) as structure-directing agent under acidic conditions [15]. This type of silica, with a defined pore framework consisting of cylindrical and parallel mesopores in the range size of 5–10 nm (interconnected or not by secondary mesoporosity and/or microporosity located in the walls), and displaying high surface area and pore volume, high hydrothermostability [16–18], received much attention

as support for NPs [19–27] or as nanocasts to obtain the corresponding negative replicas [28–31]. The particular organization of the pores allows improved control of the NPs size, dispersion, morphology, and distribution in the main or secondary pore system [32–35], while the thermal stability is much enhanced in comparison with nonsupported NPs or even those supported on ordinary silica. It should be noticed that SBA-15 with open porosity, obtained upon removal of P123 surfactant under air calcination, was usually used as support for NPs. Quite recently, the as-prepared SBA-15 was used as an organic–inorganic hybrid host to prepare nanocoatings of ZnO [36], CuO [37], and CeO₂ [38] on the internal surfaces of the mesopores. It was stated that such a hybrid material provide a unique microenvironment that consists of the confining space created between the organic template and silica walls, which, besides the high density of surface silanols, can hinder the agglomeration of the NPs into large aggregates.

So far, impregnation and precipitation have been among the most frequently used methods to prepare supported NPs. Impregnation involves the wetting of the support with the precursor solution followed by solvent removal via thermal treatment either at high temperature overnight, e.g., up to 250 °C [39], or at room temperature for a longer time (incipient wetness impregnation followed by mild drying–IWI-MD) [40]. When silica, either ordered or nonordered, is used as support, the main crystalline phase resulting from calcination under an oxidizing atmosphere consists of the corresponding metal oxides, which usually are in low interaction with the support surface. In the specific case of bicomponent NPs, the interaction between these two components is usually favored and thus NPs with different size, shape, and distribution of the two components in the same particle can be obtained [40–42]. However, the major drawback consists of the low loading degree in metal (~5 wt.%) that can be achieved, as well as the agglomeration of the NPs into more or less large bundles during the multiple thermal treatments (drying, calcination, reduction), due to limited interaction of precursors with the support surface, and consequently high mobility of the impregnated phase [40]. These shortcomings were usually overcome using precipitation, either with urea or with sodium/potassium carbonate [43–45], as a preparation method. A high loading degree in metals could be reached, ~60 wt.% or even 80 wt.% [45]. The dispersion of the metal-based NPs is much improved, while a stronger metal–support interaction is generated using these methods. Usually, upon calcination, two types of crystalline phases can be obtained, metal oxides and (phyllo)silicate (PS)-like phases. Experimental observation of a phase depends on the thermal history of the precursors. For example, copper PS-like phases are less thermally stable than nickel PS-like phases, and therefore, the probability of generating CuO by the calcination of the copper PS-like phases is higher than that of the generation of NiO during the calcination of Ni PS-like phases [46].

Recently, we reported studies of the dispersion and stabilization of copper in CuNi/SBA-15 (5 wt.% in metal) materials by IWI-MD [12,42]. Both oxide and metallic NPs manifest enhanced dispersion as well as high thermostability during the calcination and reduction processes. Taking advantage of the typical topologies of ordered supports (monomodal pore size distribution), improved thermostability was achieved by confining particles in mesospace to limit mobility of the impregnated phase and particle growth upon sintering. It was also emphasized that the active phase composition has a significant effect on the physicochemical properties of the copper–nickel-based NPs supported on SBA-15 [12]. The progressive increase in Cu/Ni weight ratio has a positive effect on the dispersion and stability of metal-derived NPs, up to a value close to 1. Further increase in this ratio, in the case of Cu/Ni to 4:1, has a negative impact on the stability and dispersion of metal

oxide phases, which appear heterogeneously distributed on the support surface, as both large bundles and mesoconfined particles. Under these circumstances, the improvement of the dispersion and stabilization of copper in copper-rich bicomponent nanoparticles is a problem that naturally arises.

In the present study, we show that the dispersion and the thermostability of copper-rich copper–nickel-based NPs (Cu:Ni weight ratio 4:1) can be enhanced by the rational selection of the support surface properties when a simple IWI-MD approach is used as preparation method. In this context, as mentioned above, SBA-15 is a versatile support offering a multitude of properties to be explored, which are related to the preparation steps. Among these properties, the chemistry of the surface is indeed very important for deposition of active metals and can be controlled by different strategies, one of them consisting of the elimination of P123 organic surfactant before impregnation. On the other hand, the preparation method plays a decisive role in the physicochemical properties of the supported NPs. So far, many studies have focused on the effect of the method of preparation of supported NPs, usually by comparing impregnation with precipitation, the main strategies used in industry to load active phases onto a solid support. Irrespective of the nature of the metal NPs, all of these studies systematically highlighted the efficiency of precipitation in terms of dispersion, loading degree, thermochemical stability and catalytic activity of the nanoparticles, in line with the above discussion [24,46–51]. However, although precipitation allows high loading degrees in metal, it involves corrosive and not environmentally friendly chemicals, as well as strictly controlled conditions for synthesis [43–45]. In addition, precipitation results in the degradation of the ordered mesoporous structure of the support. Here, we demonstrate that the use of SBA-15 with triblock copolymer P123 maintained inside the pores as an organic–inorganic hybrid support for impregnation with metal nitrates is an effective way to prepare copper-rich NPs whose dispersion and catalytic activity are higher than those prepared by precipitation. It is worth mentioning that this comparison between NPs prepared by impregnation on a partially extracted SBA-15 and by precipitation was imposed by the interactions taking place between the precursors of the active sites and the support, which are key factors in the thermal stability of the metal (oxide) NPs and their dispersion degrees. We demonstrated that such interaction is stronger for the IWI-MD/EC sample than for P/C and DP/samples due to the confinement effect of intrawall pores, which explains the higher thermostability and smaller size with higher dispersion of the NPs prepared by IWI-MD on partially extracted SBA-15 in comparison with the samples prepared by precipitation. The catalytic properties of the oxide phases were evaluated for the oxidation of CO, while metallic phases were evaluated for the hydrogenation of cinnamaldehyde in the liquid phase. The differences in the catalytic activities and selectivity are discussed in relation to the nature of metal precursors, metal–support interactions, and size and dispersion of the metal-based NPs, as well as the promoting effect of nickel on copper.

2. Experimental

2.1. Chemicals

All chemicals required to prepare the materials were used without any additional purification: tetraethylorthosilicate (Si(OC₂H₅)₄, TEOS, 98%, Aldrich), nonionic triblock co-polymer Pluronic P123 (poly(ethylene oxide)-block-poly(propylene oxide)-block-poly(ethylene oxide), EO₂₀PO₇₀EO₂₀, molecular weight 5800, BASF Corp.), copper nitrate (Cu(NO₃)₂·3H₂O, 98%, Aldrich), nickel nitrate (Ni(NO₃)₂·6H₂O, 98%, Sigma–Aldrich), urea (CH₄N₂O, SigmaUltra),

sodium carbonate (Na_2CO_3 , 99.8%, Merck), distilled water, and hydrochloric acid. The chemicals used for the hydrogenation reaction were also used as received: trans-cinnamaldehyde ($\text{C}_6\text{H}_5\text{—CH=CH—CHO}$, 98%, Merck) as reagent and isopropanol ($\text{C}_3\text{H}_8\text{O}$, 99%, Sigma–Aldrich) as solvent.

2.2. Preparation of samples

2.2.1. SBA-15 support

SBA-15 was synthesized according to a classical procedure, as proposed by Zhao et al. [15], in which 4 g of Pluronic P123 and 1.6 M HCl solution were stirred at 40 °C until the complete dissolution of the templating agent. Then 8.5 g of TEOS was added dropwise and the magnetic stirring was maintained for 24 h. The resulting gel was transferred into a polypropylene bottle and heated at 100 °C for 48 h. After filtration and drying, half of the support was subjected to calcination at 550 °C for 6 h in a muffle oven (heating ramp of 1.5 °C min^{-1}) to remove the organic template, while the other half was subjected to ethanol extraction for 5 h in order to retain only ~10% of P123 inside the pores (as confirmed by TG-DSC analysis, Fig. S1).

2.2.2. Catalysts

2.2.2.1. Incipient wetness impregnation followed by mild drying (IWI-MD). Freshly calcined and partially extracted SBA-15 supports were impregnated with an aqueous solution of the corresponding hydrated nitrates to obtain a total metal loading of 5 wt.% with Cu:Ni weight ratio 4:1. The resulting materials were gently dried at 25 °C for 5 days. The oxide phases of copper and nickel were obtained after calcination under stagnant air at 500 °C for 6 h (heating ramp 1.5 °C min^{-1}). Samples were denoted as IWI-MD/C and IWI-MD/EC for the calcined and partially extracted support, respectively.

2.2.2.2. Precipitation with Na_2CO_3 (P). The calcined SBA-15 support was dispersed in a fixed volume of 0.14 M $[\text{Cu}(\text{NO}_3)_2 \cdot 3\text{H}_2\text{O} + \text{Ni}(\text{NO}_3)_2 \cdot 6\text{H}_2\text{O}]$ aqueous solution to obtain a final metal loading of 5 wt.% with Cu:Ni weight ratio 4:1. The reaction was performed in a double-walled thermostated reactor at a temperature of 60 °C. Then 0.16 M Na_2CO_3 aqueous solution was added dropwise and stirred for 2 h. The obtained solid was separated by filtration, washed with distilled water, dried at 60 °C for 12 h, and calcined in a muffle oven at 500 °C for 6 h (heating ramp 1.5 °C min^{-1}). The resulting sample was denoted as P/C.

2.2.2.3. Precipitation with urea (DP). The calcined SBA-15 support was dispersed in a fixed volume of 0.14 M $[\text{Cu}(\text{NO}_3)_2 \cdot 3\text{H}_2\text{O} + \text{Ni}(\text{NO}_3)_2 \cdot 6\text{H}_2\text{O}]$ aqueous solution to obtain a final metal loading of 5 wt.% with Cu:Ni weight ratio 4:1. The synthesis was performed in a double-walled thermostated reactor at a temperature of 90 °C. Initially, the pH of the suspension was adjusted to 2 using a 2 M HNO_3 aqueous solution; then 3 M urea aqueous solution was added dropwise and stirred for 24 h. pH evolution was continuously monitored during the synthesis with a Hanna pH meter. During the aging step, the measured pH was 7.5 ± 0.1 . The obtained solid was separated by filtration, washed with distilled water, and dried at 60 °C for 12 h. Then it was calcined in a muffle oven at 500 °C for 6 h (heating ramp 1.5 °C min^{-1}). The resulted sample was denoted as DP/C.

2.3. Physicochemical characterization

Inductively coupled plasma optical emission spectrometry (ICP-OES) was performed on a Perkin sequential scanning spectrometer to determine the elemental composition of the catalysts

(Ni, Cu, and Si). Before analysis, a known amount of calcined sample was introduced in a diluted HF–HCl solution and then digested under microwave radiation. Powder X-ray diffraction (XRD) analysis was performed on a Bruker AXS D5005 X-ray diffractometer using Cu $K\alpha$ radiation ($\lambda = 1.54184 \text{ \AA}$) as X-ray source. For low-angle analysis, the data were collected in the 2θ range from 0.75° to 5° with a step of 0.01° (step time 10 s). For high-angle analysis, the data were collected in the 2θ range from 10° to 80° with a step of 0.05° (step time 8 s). Crystal phase identification was made by comparison with the ICDD database. Nitrogen physisorption was carried out on an Autosorb 1-MP automated gas sorption system (Quantachrome Instruments). Prior to analysis, the samples were outgassed under high vacuum at 350 °C for 3 h. The adsorption/desorption isotherms were obtained at –196 °C, allowing 4 min for equilibration between each two successive points. Textural properties were found from the isotherms using the Autosorb 1 software, version 1.55. The BET surface area was determined using the multipoint algorithm. The t -plot method was applied to quantitatively determine the micropore volumes and to assess the micropore surface areas. The mesopore size distribution was determined from the desorption branch of the isotherms using a nonlocal density functional theory (NL-DFT). High-resolution transmission electronic microscopy (HRTEM) coupled with Energy-dispersive X-ray spectroscopy (EDXS) was used to characterize the pore structure of the SBA-15 support, the distribution of NPs throughout the pores, and the microstructure of NPs, as well as their chemical composition. The micrographs were obtained on a JEOL 2100 instrument (operated at 200 kV with a LaB_6 source and equipped with a Gatan Ultra scan camera). EDXS was carried out with a Hyperline (Premium) detector (active area 30 mm^2) using the software SM-JED 2300T for data acquisition and treatment. The EDXS analysis zone is defined on the particle and generally ranges from 5 to 15 nm. Before analysis, the sample was first included in a resin and then a cut of ~100 nm width was realized by ultramicrotomy. Temperature-programmed reduction (TPR) runs were performed on an Autochem chemisorption analyzer from Micromeritics, equipped with TCD to monitor H_2 consumption and an MS detector (Omnistar, Pfeiffer) to follow possible desorption (H_2O , O_2 , CO_2) from the catalyst surface or a possible leak (N_2). The calcined samples were introduced in a U-shape microreactor and activated under 20 vol.% O_2 in N_2 flow (30 mL min^{-1}) at 500 °C for 1 h (heating ramp 5 °C min^{-1}). After cooling to 50 °C, a 3 vol.% H_2 in Ar flow was stabilized (30 mL min^{-1}) and the TPR runs were performed typically up to 900 °C (heating ramp of 5 °C min^{-1}). In situ powder XRD patterns at high angle were recorded on a Bruker D8 ADVANCE X-ray diffractometer equipped with a VANTEC-1 detector, using Cu $K\alpha$ radiation ($\lambda = 1.54184 \text{ \AA}$) as X-ray source. The calcined samples were first placed on a Kanthal filament (FeCrAl) cavity and then subjected to thermoprogrammed reduction under a 3 vol.% H_2 in He flow (30 mL min^{-1}) from 30 to 550 °C (heating ramp of 5 °C min^{-1}). The in situ diffractograms were recorded at definite temperatures in the 2θ range from 15° to 70° with a step of 0.05° (step time 2 s). Crystal phase identification was made by comparison with the ICDD database. In situ X-ray photoelectron spectroscopy (XPS) was performed before and after reduction of catalysts at 350 °C for 5 h (heating ramp 5 °C min^{-1}) under 5 vol.% H_2 /He flow (30 mL min^{-1}). The spectra were acquired with a VG Escalab220XL spectrometer from Thermo. The analysis chamber was operated under ultrahigh vacuum of $\sim 5 \times 10^{-9}$ Torr. X-rays were produced by a magnesium anode working with Mg $K\alpha$ (1253.6 eV) radiation. For the measurements, the binding energy (BE) values were referred to the Si2p photopeak at 103.8 eV. The surface Cu/Si, Ni/Si, and Cu/M atomic ratios were calculated by correcting the corresponding peak intensities with theoretical sensitivity factors based on Scofield cross sections.

2.4. Catalytic tests

2.4.1. Hydrogenation of cinnamaldehyde

For each test, the calcined catalysts were reduced under hydrogen flow (1 L h^{-1}) at $350 \text{ }^\circ\text{C}$ for 10 h (heating rate of $6 \text{ }^\circ\text{C min}^{-1}$ up to the reduction temperature). The corresponding samples are denoted as IWI-MD/R, IWI-MD/ER, P/R, and DP/R. The catalytic tests were carried out in a high-pressure Parr reactor under the following conditions: 1 mL aldehyde, 40 mL isopropanol, 0.265 g catalyst, hydrogen pressure of 10 bar, and reaction temperature of $130 \text{ }^\circ\text{C}$. Samples were periodically taken off and analyzed by GC with an HP 5890 series gas chromatograph, which is equipped with a DB-5 capillary column and a flame ionization detector. The identification of the reaction products was achieved from the retention times of pure compounds and occasionally by GC-MS (an Agilent 6890 N system equipped with an Agilent 5973 MSD detector and a DB-5-ms column). The conversion of cinnamaldehyde and the selectivity in the different hydrogenation products were calculated by taking into account the FID response factors for each compound.

2.4.2. Oxidation of CO

CO oxidation was carried out under atmospheric pressure in a quartz-glass fixed-bed continuous-flow microreactor in the temperature range $80\text{--}200 \text{ }^\circ\text{C}$. Prior to the reaction, the catalysts were pretreated at $350 \text{ }^\circ\text{C}$ under H_2 (15 mL min^{-1}) for 2 h, and then in air (15 mL min^{-1}) for 1 h. The corresponding samples are denoted as IWI-MD, IWI-MD/E, P, and DP. The catalyst (0.1 g) was contacted with a CO/O_2 mixture (total flow $55 \text{ cm}^3 \text{ min}^{-1}$; composition 1.5 vol.% CO, 1.5 vol.% O_2 , balance He). Analyses of the reaction mixture were performed on line with a HP 6890 GC equipped with a HP Poraplot Q capillary column and both a TCD and a FID (coupled with a methanator) detector. At each reaction temperature, conversions are evaluated after 30 min on stream to allow the attainment of steady-state conditions.

3. Results and discussion

3.1. Structural and textural properties of samples

The calculated values for the elemental composition of calcined copper–nickel-based samples are summarized in Table 1. It can be observed that the Cu/Ni ratios are slightly higher than those selected for preparation, indicating a small copper enrichment of the samples.

XRD patterns collected in the low-angle range for the calcined SBA-15 and copper–nickel-based materials are shown in Fig. 1. On the basis of these diffractograms, the corresponding d -spacing of the (100) plane and a_0 parameters were calculated and listed in Table 1.

As a first observation, all patterns show the three diffraction peaks indexed as (100), (110), and (200) peaks, characteristic of

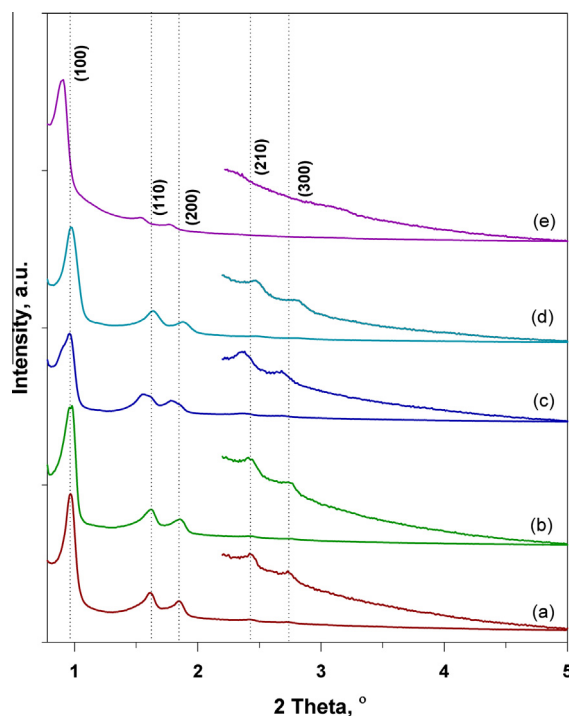


Fig. 1. X-ray diffractograms at low angle for calcined $\text{Cu}_4\text{Ni}_1/\text{SBA-15}$ prepared materials: (a) SBA-15; (b) IWI-MD/C; (c) IWI-MD/EC; (d) P/C; (e) DP/C.

2D hexagonal arrangement of pores and revealing long-range mesopore ordering [15,18]. Additionally, the presence of (210) and (300) planes is an indication of the excellent textural uniformity of the original SBA-15 as well as of $\text{Cu}_4\text{Ni}_1/\text{SBA-15}$ samples prepared by IWI-MD. No significant differences were observed for the intensities and 2θ positions of the diffraction peaks for SBA-15, IWI-MD/C, IWI-MD/EC, and P/C samples, which reveal similar orderings of the primary mesopores with comparable structural parameters. For the P/C sample, only a small attenuation of the (210) and (300) reflections is observed, suggesting a partial loss of the long-range order in the final material.

For the DP/C sample, these two reflections can no longer be observed. In addition, the intensity of the (100) reflection decreases, while the corresponding 2θ position is shifted to lower values, indicating larger mesopores and higher d -spacing and cell parameter. Additionally, the intensity of the diffraction peaks at higher 2θ is also decreased up to disappearance. Consequently, the precipitation with urea induces significant changes in the structural characteristics of the support. A partial collapse of the ordered mesoporous structure of the SBA-15 support, due to the partial dissolution of the silica walls, can be proposed to be the origin of these results. Similar behavior was previously observed for cobalt deposition on SBA-15 by precipitation with urea, confirming that harsh conditions such as pH and temperature can partially damage the mesostructure of the support [46].

XRD patterns recorded for the calcined materials from 20° to 80° 2θ are depicted in Fig. 2. The X-ray diffractogram for the IWI-MD/C sample shows small diffraction peaks characteristic of cubic NiO (ICDD 047-1049) and sharper diffraction peaks characteristic of monoclinic CuO (ICDD 048-1548), indicating smaller crystallites of NiO than those of CuO. The average sizes of metal oxide crystallites, d_{NiO} and d_{CuO} , estimated from peak broadenings, are 29.5 and 14.5 nm, respectively. This result suggests that an important part of the metal oxide precursors are transported outside the pores of SBA-15 during thermal activation. It is interesting to note that for the IWI-MD/EC sample, prepared by IWI-MD on partially

Table 1

Chemical composition and structural properties of the calcined support and $\text{Cu}_4\text{Ni}_1/\text{SBA-15}$ samples.

Sample	Cu–Ni ^a (wt.%)	d_{100} ^b (nm)	a_0 ^c (nm)
SBA-15	–	9.1	10.5
IWI-MD/C	5.1–1.1	9.1	10.5
IWI-MD/EC	4.3–0.9	9.1	10.5
P/C	4.5–0.9	9.1	10.5
DP/C	4.9–1.1	9.8	11.3

^a Metal content by ICP-OES.

^b d_{100} = lattice spacing obtained by low-angle XRD.

^c a_0 = unit cell parameter calculated using the equation $a_0 = 2d_{100}/\sqrt{3}$.

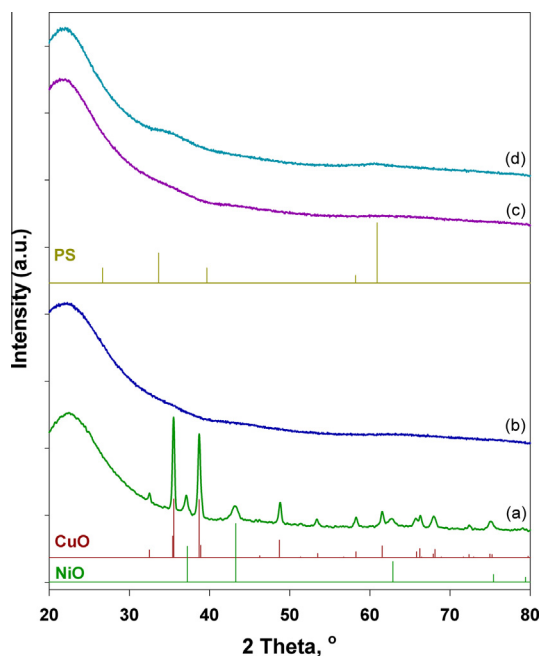


Fig. 2. X-ray diffractograms at high angle for calcined $\text{Cu}_4\text{Ni}_1/\text{SBA-15}$: (a) IWI-MD/C; (b) IWI-MD/EC; (c) P/C; (d) DP/C.

extracted SBA-15, the XRD pattern does not show diffraction peaks associated with either Ni oxide or Cu oxide, clearly indicating (i) an excellent dispersion of the crystalline phases, with size below the XRD detection limit (~ 3 nm) and (ii) a crucial role of residual organics from P123 in the dispersion of metal precursors. So far, different strategies have been proposed for preparing finely dispersed NPs, but they are usually complicated and involve several steps, among them the functionalization of the surface with hydrophilic or hydrophobic organic groups, as well as the use of toxic organic solvents or even organometallic precursors, making them unsustainable [32,33,52–55]. The approach consists in the modification of support surface properties, grafting/encapsulating functions having more affinity with the ionic species in solution. In strong interaction with the support surface, surface species mobility is reduced during thermal treatment, and consequently, increased dispersion of the active phases can be achieved. In this context, the use of SBA-15 silica containing mesopores occluded with residual P123 triblock copolymer as a functional support is highlighted as an efficient preparation method to improve the dispersion of transition metal (oxide) NPs.

Improvement of the dispersion of NPs deposited on partially extracted SBA-15 can be explained by taking into consideration two aspects:

- First, by using the support without calcination, the framework contraction due to the surface dehydroxylation and formation of siloxane bond is avoided, while the concentration of surface silanols is maintained at high levels (Si-OH , 4.7 mmol g^{-1}) [56,57].
- Second, the presence of the organic surfactant having hydrophilic PEO groups embedded in the walls creates a confining space between the template and the silica walls that limits the mobility and growth of the metal precursors within the mesopores during thermal steps [37,58]. Therefore, a tandem effect of (i) the silanols, which stabilize the inorganic precursor of the metal, and (ii) the confining space within the mesopores, allowing the high dispersion of the very small metal (oxide) NPs, could be assumed.

These assumptions appear to be reasonable, since the corresponding XRD patterns do not display reflections of any crystalline phase, suggesting a high distribution of the oxide phase throughout the silica porosity. Interestingly, this level of metal oxide distribution is very similar to those obtained by the precipitation of the metallic cations from the corresponding nitrate salts either with sodium carbonate (P/C sample) or urea (DP/C sample) (Fig. 2). However, for the DP/C sample, very large diffraction peaks can be distinguished at $2\theta \sim 35^\circ$ and 60° . These reflections are attributed to (phyllo)silicate-like phases, as generally reported by precipitation with urea on silica [43,44]. Taking into account the weight ratio between copper and nickel (4:1), these reflections could eventually be associated with a residual highly dispersed copper (phyllo)silicate-like phase (Cu-PS). Ni-PS-like phases could also form, but they are difficult to observe by XRD due to the small amount of nickel (Table 1). It is worth mentioning that, irrespective of the preparation method, after calcination, bicomponent metal oxide nanoparticles with size below the XRD sensitivity and very well distributed in the solid support are obtained, except for the IWI-MD/C sample.

Textural properties of the calcined SBA-15 and copper–nickel-based materials were assessed by nitrogen physisorption. The corresponding adsorption/desorption isotherms, as well as the pore size distribution curves, are illustrated in Fig. 3. It can be noticed that the isotherms of the original SBA-15 and copper–nickel-based materials prepared by IWI-MD, either on calcined or on partially extracted support, are very similar. They are of type IV with hysteresis loop of type H1, which are characteristic, of mesoporous materials with cylindrical and parallel pores [15,18].

It is evident that the impregnation of SBA-15 solids followed by drying and calcination did not change the mesostructure of the support. Moreover, the parallel hysteresis branches indicate the absence of pore plugging by oxide NPs, usually evidenced by a new maximum in the pore size distribution curves [59]. The curves drawn in Fig. 3 for these three samples display only the maximum corresponding to the size of the main mesopores (i.e., 8.4 nm) of the initial SBA-15 support. The sample obtained by carbonate precipitation exhibits an isotherm of type IV, but the hysteresis loop changes from H1 to H2 type. Moreover, the relative pressure associated with the capillary condensation in mesopores shifted to lower values (0.5–0.8) in comparison with the support (0.65–0.8). These results indicate the modification of the topology of the mesopores, as well as a slight broadening of the pore size distribution. H2-type hysteresis observed for the P/C sample could be explained by a local structural disorder of the mesoporosity as a result of the very slight acidic pH of the synthesis mixture (~ 6.5). However, this result, besides XRD at high angle, indicates high dispersion of Cu and Ni metal precursors, since the hysteresis shape does not indicate any constriction in the pores. An isotherm of type IV, typical of mesostructured materials, is also obtained for the DP/C sample. However, the significant changes in either the isotherm or hysteresis shape and position indicate a significant alteration of the ordered mesopore structure at long range, confirming XRD results at low angle [47,60]. The isotherm revealed two distinct stages of capillary condensation at relative pressures (p/p_0) ~ 0.6 – 0.8 and ~ 0.8 – 0.95 , respectively, suggesting a bimodal pore size distribution in the material. Indeed, the corresponding pore size distribution (PSD) curve shows a very wide pore size distribution with two visible maxima, at 8.1 and ~ 15 nm, respectively. The first appears to be a remnant of the primary mesopores of the parent SBA-15, while the second originates from much larger pores generated by a dissolution–reprecipitation process in a slightly alkaline medium (pH ~ 7.5) and a high temperature of synthesis (90°C) applied for the precipitation step. On the basis of the isotherms in Fig. 4 and applying specific algorithms,

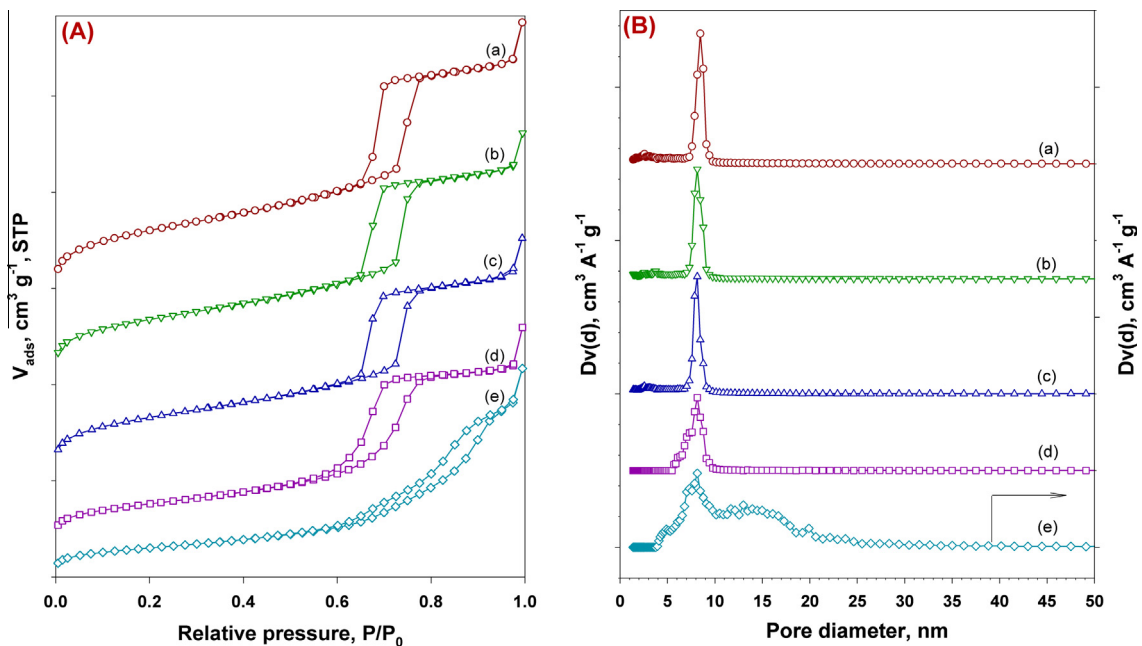


Fig. 3. N_2 physisorption isotherms of calcined $Cu_4Ni_1/SBA-15$: (a) SBA-15; (b) IWI-MD/C; (c) IWI-MD/EC; (d) P/C; (e) DP/C.

the textural properties of the investigated materials were evaluated and they are summarized in Table 2. When compared with SBA-15 support, all copper–nickel-based samples show lower values of the main textural properties, these changes having different reasons, as explained further. For P/C and DP/C samples, the decrease of the calculated values is also correlated with the partial disordering of the mesostructure, which obviously depends on the pH value. As a consequence, the DP/C sample manifests a much greater decline of the mesostructure due to the harsher conditions applied, as already mentioned. For the samples prepared by impregnation (i.e., IWI-MD/C and IWI-MD/EC), the decrease of the values of the textural properties is attributed to the deposition of the metal oxide phase inside the mesopores (IWI-MD/EC) or at the pore opening (IWI-MD/C).

The additional decrease of the micropore-related textural values (surface and volume) could suggest their blocking with metal precursors homogeneously distributed in mesopores and/or deposition of precursors even in intrawall pores. For the samples prepared by precipitation methods, the decline of the microporosity could also be a consequence of structural order loss, as identified by XRD at low angle. The results obtained by nitrogen physisorption, which are basically in good agreement with the XRD results at low angle, besides those provided by XRD at high angle, indicate that IWI-MD is an effective method of preparing (bi)metallic NPs supported on SBA-15 silica occluded with P123, with excellent textural uniformity and dispersion of the metal precursors similar to that obtained by precipitation. In light of these results, it can be stated that the precipitation methods, especially DP, are less effective because they lead to mesostructure alteration.

The morphology and size of nanoparticles, as well as their location with respect to the mesopores, were further analyzed by TEM at low and high magnification. Representative TEM images of calcined materials prepared by IWI-MD, P, and DP are shown in Fig. 4.

In total agreement with XRD and N_2 physisorption, different qualities of mesostructures can be observed depending on the preparation method.

First, TEM images corresponding to the IWI-MD/C sample (Fig. 4A) show the typical mesoporous structure of SBA-15 with

an excellent long-range order of the cylindrical mesopores. Second, three kinds of metal oxide NPs can be observed.

Therefore, part of the metal oxide phase forms very large aggregates ~ 80 nm in size, stabilized at the mesopore openings. Another part forms aggregates 80–100 nm in size on the external surface of the SBA-15 grains. A small part of the metal oxide phase is confined within the mesopores and generates nanobundles as a result of mass transfer through the micropores interconnecting the adjacent mesopores (Fig. 4A). As a general trend, the high proportion of copper (Cu:Ni = 4:1) has a negative effect on the size and dispersion of the metal oxide phases when calcined SBA-15 silica is used as support. Similar results were previously discussed in a study focusing on the effect of chemical composition on the morphostructural properties of copper-containing NPs confined and stabilized within the channels of ordered SBA-15 silica by the IWI-MD approach [12].

From XRD and N_2 -physisorption results, partially extracted SBA-15 silica is more appropriate as a support, providing a more favorable microenvironment for impregnation, consisting of a higher density in surface silanol and a confined space inside the mesopores. Indeed, TEM images collected for this sample (Fig. 4B) confirm these results. The hexagonal arrangement of mesopores is well observed, while no external NPs can be detected throughout the observed zones. Apparently, the mesopores are empty of particles. However, at high resolution, very small (~ 2 nm) and darker spots (such as those indicated by arrows) appear highly dispersed along the mesochannels. These particles cannot be detected by XRD due to their small size, while the obstruction of the primary mesopores is circumvented (due to the absence of aggregation). Punctual EDX microanalysis (either with a large analysis zone over silica grains or a focalized 5–10 nm zone) evidenced copper and nickel in a ratio close to that assessed by ICP, indicating a homogeneous dispersion of the two elements inside the support.

TEM images recorded for the P/C sample (Fig. 4C) reveal a material that consists of mesochannels with local discontinuities, as suggested by XRD at small angle and N_2 physisorption. The diameter of the mesopores determined by TEM (~ 7 –8 nm) is in full agreement with the average pore diameter determined by N_2

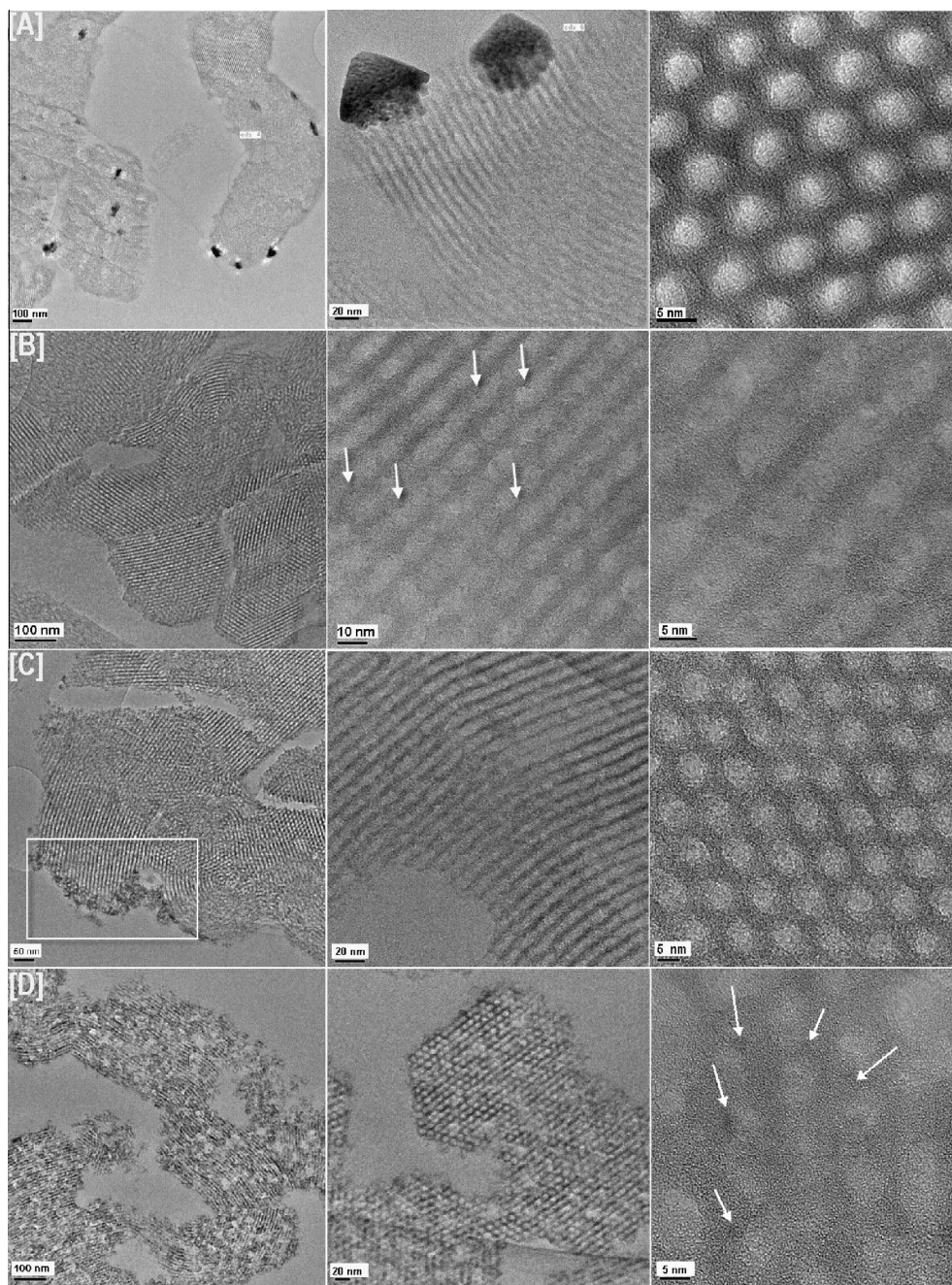


Fig. 4. TEM images at low and high resolution for calcined $\text{Cu}_4\text{Ni}_1/\text{SBA-15}$: (A) IWI-MD/C; (B) IWI-MD/EC; (C) P/C; (D) DP/C.

physisorption and NL-DFT calculation (predominantly 8.4 nm, minor 7.4 nm). Concerning the metal-based NPs, finely dispersed metal precursors (area marked with rectangle) can be observed toward the external surface, most likely in the form of Cu and Ni oxide phases generated by calcination. Indeed, according to EDX microanalysis, these phases are characterized by a $(\text{Cu} + \text{Ni})/\text{Si}$ atomic ratio almost four times higher than that corresponding to that determined by ICP (0.53 vs. 0.15), showing an enrichment in the active phase in these areas. In addition, the $\text{Cu}/(\text{Cu} + \text{Ni})$ atomic ratio, determined by EDX, is nearly identical to that determined by ICP (0.85 vs. 0.82), indicating homogeneous dispersion of the two metal precursors in these areas. However, by analyzing several TEM images, it can be concluded that, although observed, these external oxide phases do not represent a major phase. The phases containing the metal precursors are mainly

located inside the pores of SBA-15, while the emerged NPs are too small to be easily observed in the collected images. Copper and nickel were detected only by EDX microanalysis performed on different areas of the sample (Fig. S2).

In agreement with XRD at low angle and N_2 physisorption results, TEM images recorded for the DP/C sample (Fig. 4D) confirm the significant alteration of the SBA-15 mesostructure, with creation of bimodal porosity (formation of large pores created by a dissolution–reprecipitation process occurring during synthesis). Additionally, neither metal precursor phases on the external surface nor crystalline phases of large size are observed, indicating high dispersion of metal phases. Even at high resolution, the detection of the transition metals containing particles is difficult. Hence, the presence of the two elements in the silica grains was proved by EDX microanalysis in multiple areas, confirming the excellent

Table 2
Textural properties of the calcined supports and Cu₄Ni₁/SBA-15 samples.

Sample	S_{BET} (m ² /g) ^a	S_{micro} (m ² /g) ^b	V_{pore} (cm ³ /g) ^c	V_{micro} (cm ³ /g) ^d	D_p (nm) ^e
SBA-15	816	183	1.19	0.082	8.4
IWI-MD/C	717	142	1.06	0.063	8.4
IWI-MD/EC	699	156	1.01	0.069	8.4
P/C	458	25	0.87	0.009	7.4; 8.4
DP/C	323	11	0.84	0.003	8.4, 15.0

^a S_{BET} = total specific surface area obtained by BET equation.

^b S_{micro} = micropore surface area obtained by *t*-plot method.

^c V_{total} = total pore volume measured at $p/p_0 = 0.97$.

^d V_{micro} = micropore volume obtained by *t*-plot method.

^e D_p = pore size determined by NL-DFT algorithm.

homogeneity of the cation dispersion into support mesoporosity, with a measured (Cu/(Cu + Ni)) atomic ratio in agreement with that determined by ICP (0.85–0.88 vs. 0.80).

3.2. Reducibility and evolution of crystal phases upon reduction under hydrogen

The reducibility and nature of the generated metallic phases upon synthesis and calcination, as well as the metal–metal and metal–support interactions, were investigated by TPR. The recorded reduction profiles are displayed in Fig. 5.

The TPR profile for the IWI-MD/C sample shows a maximum at 325 °C. Usually, the reduction of bulk CuO takes place in the range from 250 to 325 °C, with a maximum at ~280 °C [61]. The slight shift of the reduction temperature toward higher values, as well as the breadth of the corresponding peak in Fig. 5a suggest a large distribution of particle sizes [62] that are probably involved in different interactions with silica (i.e., from no to weak interactions),

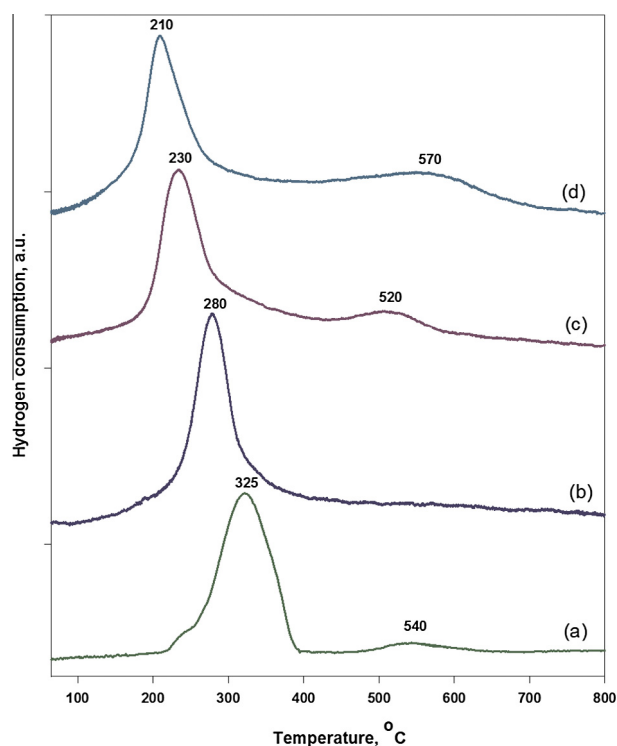


Fig. 5. TPR profiles for calcined Cu₄Ni₁/SBA-15: (a) IWI-MD/C; (b) IWI-MD/EC; (c) P/C; (d) DP/C.

but also with nickel. A small peak with $T_{\text{max}} \sim 540$ °C can be associated with the reduction of Ni²⁺ (NiO phase). Since the reduction of bulky NiO takes place at temperatures below 420 °C [63], it is assumed that a reduction at 540 °C corresponds to NiO confined to mesopores and/or in interaction with the support. According to the TEM analysis for this sample, a small part of the formed metal oxides are confined within the mesopores of SBA-15 silica and could explain this reduction at high temperature. Additionally, two shoulders can be observed at 240 and 350 °C. The first could be attributed to the reduction of Cu²⁺ (from CuO) with relatively high dispersion, probably CuO involved in the confined nanoparticles observed in TEM images. The second could be attributed to the reduction of both cations, Cu²⁺ and Ni²⁺, in CuO and NiO in interaction with each other. This complex TPR profile, displaying different reduction temperatures, reveals a heterogeneous distribution of the oxides in this material, thus sustaining TEM analysis results that showed different distributions of the metal oxides after impregnation of the calcined SBA-15, drying, and calcination.

The TPR profile for IWI-MD/EC is less complex, showing a single reduction peak, i.e., $T_{\text{max}} = 280$ °C. Although this reduction temperature would indicate a bulk copper oxide, this is unlikely, since a very high dispersion for the copper phase is clearly shown by the other analyses (i.e., XRD, TEM). The peak is narrower in comparison with that obtained for the IWI-MD/C sample, indicating much improved dispersion of the bicomponent copper-rich nanoparticles, which are smaller and with enhanced homogeneity over their size [62]. Since the reducing cations are included in bicomponent NPs, a strong metal–metal interaction could be considered, as well.

For the samples prepared by precipitation methods (i.e., P/C and DP/C), TPR profiles are different from those recorded for the samples obtained by impregnation. Two maxima for the consumption of hydrogen are observed. The first maximum is located at 230 and 210 °C for P/C and DP/C, respectively. This hydrogen consumption is associated with the reduction of Cu²⁺ to Cu⁰ in the CuO phase generated by the decomposition, during calcination at 500 °C, of (phyllo)silicates-like phases formed due to the synthesis process. As noticed, these maxima are shifted toward much lower temperatures in comparison to IWI-MD samples, due to the high dispersion of the generated phases [64–67]. The second peaks are located at 520 and 570 °C for P/C and DP/C, respectively, the peak corresponding to the DP/C sample being much larger than that for the P/C sample. These temperatures are usually associated with the reduction of nickel in strong interaction with the support, as in (phyllo)silicates-like phases [46–68]. Additionally, a two-steps reduction of copper in residual PS-like phases [PS → Cu⁺ (>200 °C) and Cu⁺ → Cu⁰ (>600 °C)] could be also considered for the DP/C sample [64].

As a conclusion for TPR investigation, it can be pointed out that the samples prepared by impregnation show mainly metal–metal interactions, while those prepared by precipitation methods are mostly characterized by metal–support interactions, both kinds of interactions directly affecting the metal precursor size, dispersion, and reducibility.

In order to clarify the intermediate crystalline phases formed during the reduction process, as well as their thermal stability, the calcined IWI-MD/EC, P/C, and DP/C samples were reduced at different temperatures under hydrogen and monitored in situ by XRD. The corresponding XRD patterns are illustrated in Fig. 6. Note that IWI-MD/C was not investigated by this technique due to the poor homogeneity of the oxide phase in the final solid.

For IWI-MD/EC and P/C samples, and irrespective of the reduction temperature, XRD patterns show diffraction lines attributed only to the Kanthal holder. No significant sintering of the phase can be detected until 550 °C, and formed phases remain very small.

For the DP/C sample, XRD performed after reduction at 30 °C displays the same phase as detected by ex situ XRD analysis, that

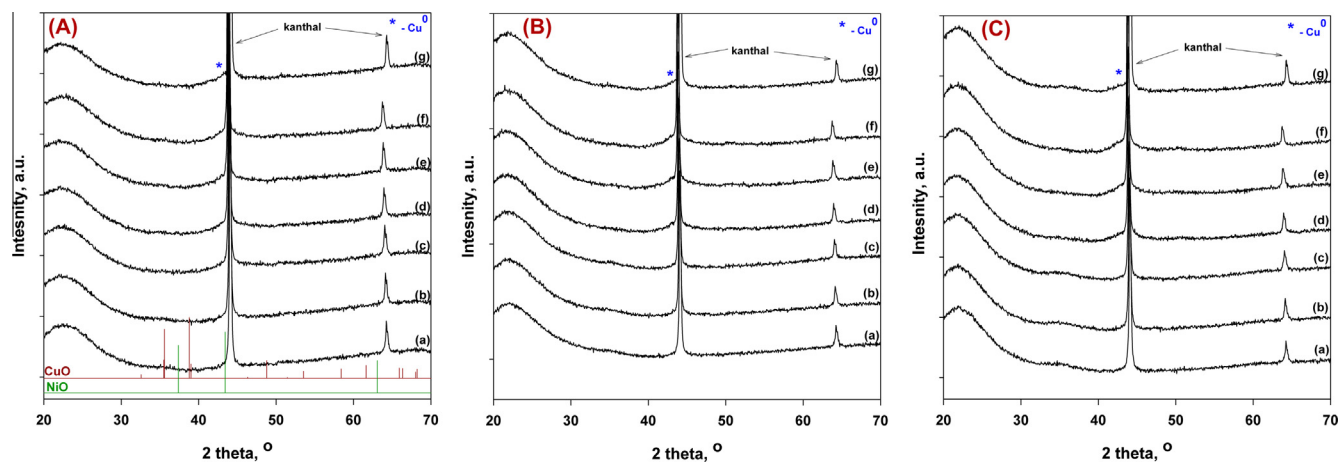


Fig. 6. In situ XRD patterns for (A) IWI-MD/EC, (B) P/C, and (C) DP/C after reduction under hydrogen at different temperatures: (a) 30 °C, (b) 150 °C, (c) 250 °C, (d) 350 °C, (e) 450 °C, (f) 550 °C, (g) 30 °C.

is, a residual Cu-PS-like phase. As the temperature increases, the corresponding diffraction peaks become smaller; after reduction at 350 °C, they are very difficult to distinguish. When the temperature is further raised to 450 °C, these peaks disappear, indicating their complete reduction to the metallic phase and their low thermostability, as already discussed in the TPR section. A very broad and small peak can be observed at $2\theta \sim 43.4^\circ$ due to the diffraction of the (111) plane of metallic Cu^0 (JCPDS 04-0836) when the reduction temperature exceeds 350 °C. It became sharper as the temperature increases, suggesting minor sintering of the metallic copper. However, even after reduction at 550 °C, this peak, although more outlined in comparison to reduction at 350 °C, is still broad and small, making difficult the estimation of the average crystal size by the Scherrer equation. Interestingly, when these XRD patterns are compared with those collected for the IWI-MD/EC sample, no traces of metallic copper can be distinguished in the XRD patterns for the last sample, even after reduction at 550 °C. Hence, the high dispersion of the oxide NPs obtained from the partially extracted SBA-15 support not only was confirmed, but also results show that NPs' thermostability exceeds that manifested by the DP-derived material. Thus, (i) the role of P123 in NPs stabilization and (ii) the advantage brought by the IWI-MD method when a suitable support is used to prepare highly dispersed and thermostable supported NPs were validated. Consequently, the microenvironment generated at the interface between the silanol-rich inorganic surface and the pore-occluded residual template impact positively not only the dispersion but also the thermostability of NPs.

Due to the fact that the identification of the metallic NPs was difficult to perform by XRD, TEM analysis was also carried out for the three samples after reduction at 550 °C. Representative images are depicted in Fig. 7.

For the samples prepared by precipitation (P/C and DP/C), dark spots can be observed along the mesochannels or even in the walls (indicated by white arrows in Fig. 7B and C). The very small size of the particles, in addition to the low contrast with silica, makes the measurement of particles difficult. Even under these conditions, the size distribution was estimated for 70 particles from different images taken at high resolution. Even if it is below the recommended confidence particle number (200 particles), this distribution reflects the size of visible particles by TEM. Values of 2.99 and 2.29 nm were calculated for the average sizes of the nanoparticles in P/C and DP/C samples, respectively, consistent with data obtained by in situ XRD. Interestingly, for the IWI-MD/EC sample, the emerged metallic NPs are not directly observed, even at high

resolution, the presence of transition metal in the particles being confirmed by EDX spectroscopy. However, the oxide nanoparticles can easily be observed on the wall surface of the primary mesochannels (Fig. 4B and related discussion). Since no visible deterioration of the mesopores can be noticed for the reduced materials, a mass transfer from the main mesopores to intrawall pores located nearby can be proposed to explain the migration of the precursor and the lack of metallic particle formation at the primary mesopore surface after reduction. Because NPs are very difficult to see under these conditions, this sample was exposed to a strong electron beam in the microscope for a period long enough to destroy the porous network of SBA-15, while increasing the contrast between silica and NPs. This interesting method was previously proposed to detect small NPs that are particularly confined in intrawall pores of SBA-15 [32]. Representative images are depicted in Fig. 8.

In the first image, the pores appear empty of particles, while some gray spots can hardly be distinguished in the walls. After exposure to an electron beam for 3 min (Fig. 9B), the ordered mesostructure appears partially damaged, while the nanoparticles are still not very clearly seen. Only after 6 min of exposure (Fig. 9C) does the ordered pore structure appear completely destroyed, and uniform nanosized particles emerge in the TEM images. The particle size was possible thereafter to measure from such images (the corresponding histogram is provided in Fig. 7A). An average size of 1.33 ± 0.64 nm was obtained for this sample. It should be mentioned that a slight overestimation of the particle size could not be excluded as a result of the bombardment, which is known to result in particle sintering. This observation strongly supports the idea that using a simple method such as impregnation over partially extracted SBA-15, without a support surface postfunctionalization step, the copper-based nanoparticles can be selectively located in the intrawall porosity of the SBA-15.

3.3. Surface chemical states of samples

The surface composition and chemical states of copper and nickel for the calcined and reduced samples were investigated by XPS analysis. The binding energies (BE) and the atomic ratios at the sample surfaces are listed in Table 3. The corresponding spectra are provided in Figs. S3–S6.

For the IWI-MD/C sample, two BE at 933.6 and 855.7 eV attributed to the oxidation states of Cu^{2+} and Ni^{2+} in CuO and NiO phases, respectively, were identified in the XPS spectra. These values are close to that reported for the corresponding bulk CuO

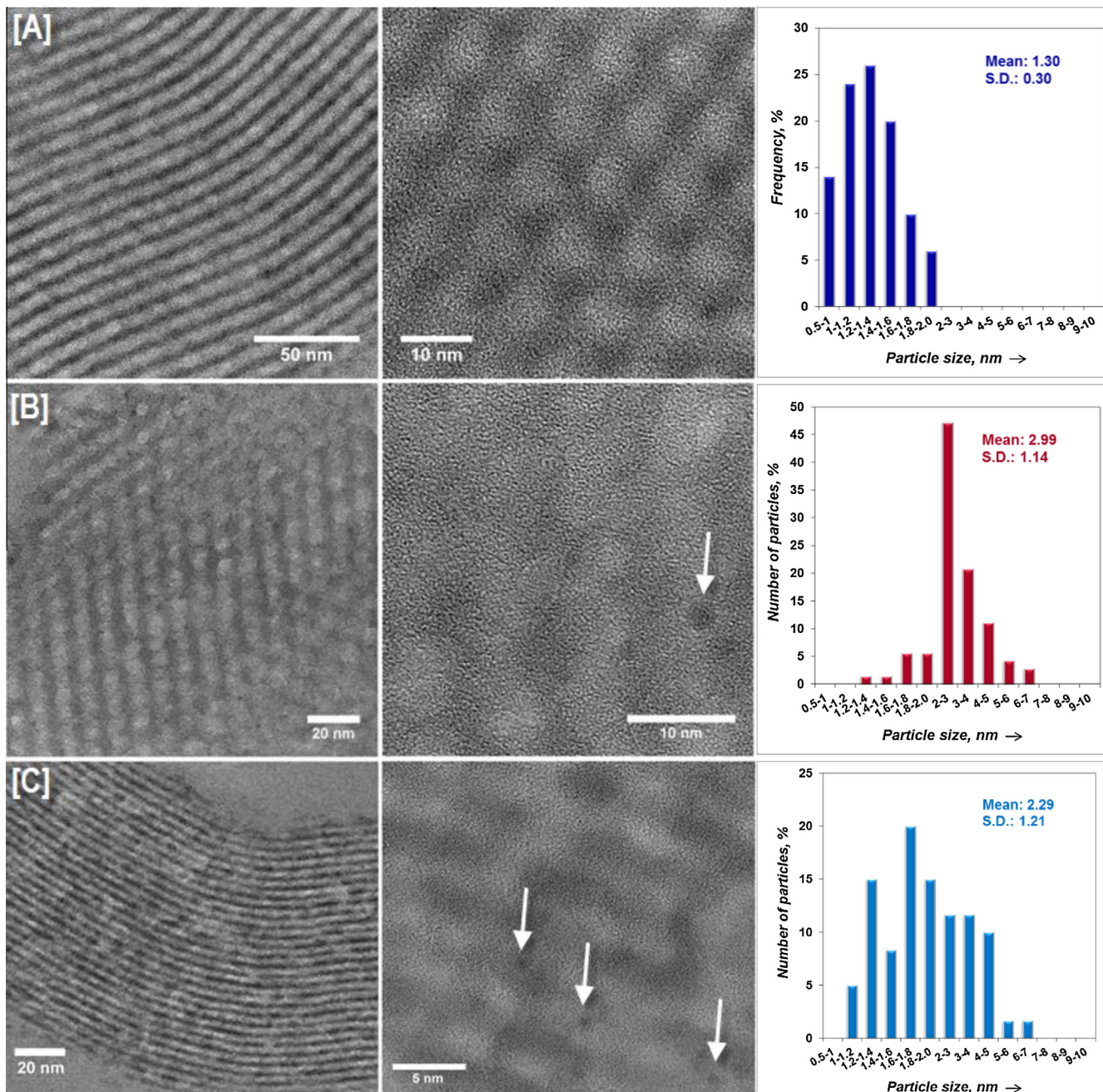


Fig. 7. TEM images for (A) IWI-MD/EC, (B) P/C, and (C) DP/C after reduction under hydrogen at 550 °C and the corresponding particle size distributions.

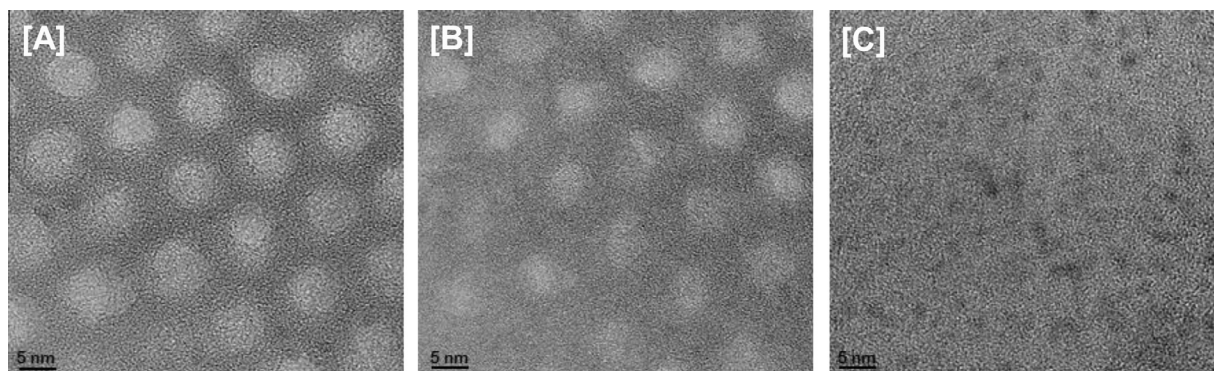


Fig. 8. HRTEM images of IWI-MD/EC sample before (A) and after exposure to strong electron beam for 3 min (B) and 6 min (C).

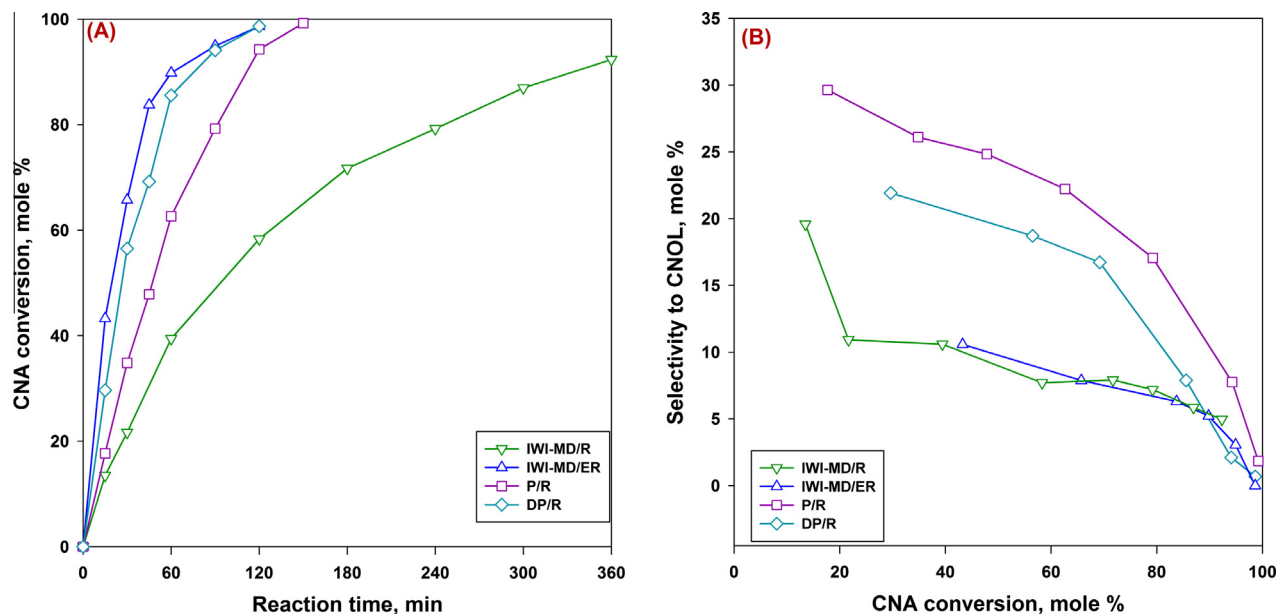


Fig. 9. CNA conversion vs. reaction time (A) and selectivity to CNOL vs. CNA conversion (B) for $\text{Cu}_4\text{Ni}_1/\text{SBA-15}$. Test conditions: $T_{\text{reduction}} = 350\text{ }^\circ\text{C}$; $T_{\text{reaction}} = 130\text{ }^\circ\text{C}$; 0.265 g catalyst; 1 mL of CNA; 40 mL isopropanol as solvent; 10 bar H_2 ; stirring rate 900 rpm.

Table 3

XPS results for calcined and reduced $\text{Cu}_4\text{Ni}_1/\text{SBA-15}$ samples.

Sample	$\text{Cu}2p_{3/2}$ (eV)	$\text{Ni}2p_{3/2}$ (eV)	Cu/Si^a	Ni/Si^a	Cu/M^a
<i>Calcined materials</i>					
IWI-MD/C	933.6	855.7	0.011 (0.051)	0.014 (0.012)	0.441 (0.810)
IWI-MD/EC	933.6; 936.0	857.2	0.030 (0.045)	0.010 (0.010)	0.744 (0.818)
P/C	933.6; 936.0	857.0	0.039 (0.048)	0.015 (0.010)	0.716 (0.820)
DP/C	933.9; 936.0	856.9	0.102 (0.052)	0.033 (0.013)	0.753 (0.800)
	$\text{Cu}2p_{3/2}$ (eV)	$\text{Ni}2p_{3/2}$ (eV)			
	Cu^0	Ni^{2+}	Ni^0		
<i>Reduced materials at 350 °C</i>					
IWI-MD/R	932.2	855.7	0.005 (0.051)	0.006 (0.012)	0.462 (0.810)
IWI-MD/ER	932.8	857.1	0.023 (0.045)	0.008 (0.010)	0.740 (0.818)
P/R	933.0	857.2	0.026 (0.048)	0.014 (0.010)	0.654 (0.820)
DP/R	932.8	857.0	0.053 (0.052)	0.030 (0.013)	0.637 (0.800)

^a Surface atomic ratios and bulk atomic ratios (in parentheses); M = Cu + Ni.

(~933.5 eV [69]) and greater than that of bulk NiO (~854.9 eV [70]). Accordingly, copper is poorly dispersed and in weak interaction with silica, while nickel is better dispersed and in strong interaction with silica. The value of BE for nickel is very close to that usually reported for Ni^{2+} in phyllosilicate-type phases [71,72] supporting the formation of such phases even for IWI-MD/C material, although these phases were not detected by the other investigation techniques. This result is, however, not very surprising, since our previous studies on copper–nickel bimetallic NPs supported on SBA-15 clearly showed the formation of Ni PS-like [12,40]. Additionally, changes in $\text{Ni}2p_{3/2}$ BE can also be correlated with the *d–d* band interactions between nickel and copper atoms in close vicinity to each other [70].

For the other three samples, two binding energies were identified for Cu^{2+} after curve fitting. The first (933.6/933.9 eV) makes an insignificant contribution and corresponds to that of CuO in weak interaction with silica. This is likely to occur due to (i) the larger amount of copper than nickel in all these samples and (ii) the mobility of the copper species, which makes difficult to stabilize them with strong interaction with support surface [60]. The second (936.0 eV) represents the major contribution to the Cu^{2+} signal. The position suggests either a high dispersion of the copper phase

(IWI-MD/EC) [73–77] and/or a strong copper–silica interaction as in (phyllo)silicate phases (P/C and DP/C), in line with the TPR data [78]. For Ni^{2+} , the evaluated BEs are higher than that of Ni^{2+} in the IWI-MD/C sample, indicating a higher dispersion of nickel phases as well as stronger nickel–silica interactions [79–82].

The XPS quantitative data are listed in Table 3. For the IWI-MD/C sample, a large decrease of the Cu/Si ratio at the surface, in comparison with the bulk composition, was observed, which is in line with the observed heterogeneous distribution of the metal oxide NPs in the sample. For the IWI-MD/EC and P/C samples, the Cu/Si ratio is closer to the bulk ratio, suggesting a more homogeneous distribution of copper in these two samples, while for DP/C sample this ratio is higher than the bulk ratio value, indicating a slight enrichment in copper at the sample surface. As concerns the Ni distribution in the IWI-MD/C sample, an enhanced Ni proportion on the surface is assumed on the basis of the higher value for Ni/Si measured by XPS than by ICP. For the IWI-MD/EC sample, Ni/Si ratios on the surface and in the bulk are identical, proving the homogeneous distribution of this element on the sample surface. For samples prepared by precipitation methods, an increase of Ni/Si calculated by XPS can be observed as a result of the surface enrichment in Ni.

Cu/M ratios calculated by XPS show that most of the Ni is located in the near-surface region of IWI-MD/C, while for the other three samples, the Cu/M ratio on the surface is slightly lower than the bulk value, indicating a slight enrichment in nickel at the surface. Therefore, according to ICP, XPS, and TEM, different distributions of the two elements (Cu and Ni) in the four samples, related to the preparation method, the nature of the support (calcined or partially extracted), and metal–support and metal–metal interactions, can be recognized.

After reduction at 350 °C, the binding energies for copper are shifted to lower values due to the reduction of Cu^{2+} to Cu^0 [70,83]. Interestingly, almost similar values are obtained for IWI-MD/R and P/R, i.e., 933.2 and 933.0 eV, respectively, while for IWI-MD/ER and DP/R the same value was assessed for both of them, 932.8 eV. As noticed, for the last two samples, the binding energies are lower than for the first two samples, indicating electron transfer between nickel and copper, which are in strong interaction [83]. For nickel, two binding energies were identified in the spectra collected for all samples. The first is almost similar to that obtained for the calcined samples, meaning that there is incomplete reduction of surface nickel at this temperature, a result supported by TPR. The second binding energy value (852.6–853.0 eV) is lower than the first one and is characteristic of metallic Ni^0 [70,83]. As a general trend, the M/Si and Cu/M ratios are maintained at values almost similar to those for the calcined samples, suggesting that the distribution of elements is not significantly changed after reduction, and thus confirming the good stability of NPs toward thermal sintering.

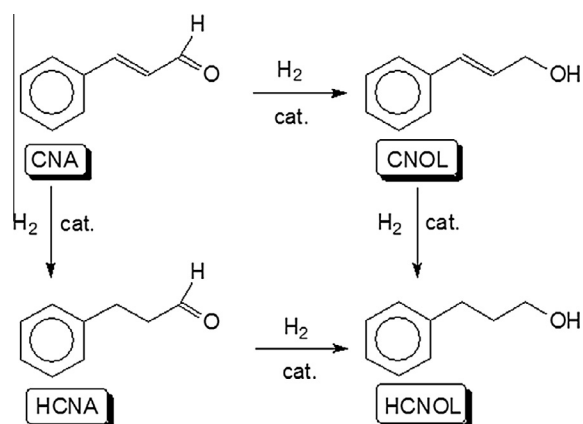
3.4. Catalytic properties of oxide and metallic materials

3.4.1. Hydrogenation of CNA, metal phase accessibility, and metal–metal/metal–support interaction

After reduction at 350 °C under H_2 flow, the catalytic performances of $\text{Cu}_4\text{Ni}_1/\text{SBA-15}$ materials were evaluated for the hydrogenation of cinnamaldehyde (CNA) in liquid phase at 130 °C under 10 bar of H_2 . The hydrogenation of CNA takes place in two steps (Scheme 1).

First, the partially hydrogenated products, cinnamyl alcohol (CNOL) and hydrocinnamaldehyde (HCNA), are produced. These two compounds are hydrogenated further to the saturated alcohol, hydrocinnamyl alcohol (HCNOL).

Fig. 9A shows the variation of the total conversion of CNA depending on the reaction times for all catalysts. As a first observation, the sample prepared by IWI-MD on calcined SBA-15 (IWI-MD/R) is less active (CNA conversion of 90% in 360 min of reaction), while the samples prepared by IWI-MD on partially extracted



Scheme 1. Reaction pathways for the hydrogenation of can.

SBA-15 (IWI-MD/ER) and by deposition–precipitation (DP/R) are the most active (CNA conversion of 100% in 120 min of reaction).

This significant increase in catalytic activity can be attributed to a large number of accessible active sites, characterized by a higher dispersion of Cu^0 and Ni^0 [13,84,85]. Regarding the catalytic activity of samples prepared by precipitation with Na_2CO_3 (P/R), lower activity than for DP/R is measured. This is in line with XPS data (see the Cu/Si and Ni/Si surface atomic ratios in Table 3), which show a smaller amount of metallic active phases on the P/R surface in comparison with the surface of DP/R.

Fig. 9B shows the selectivity of $\text{Cu}_4\text{Ni}_1/\text{SBA-15}$ materials to CNOL as a function of the conversion of CNA. Both samples prepared by IWI-MD, irrespective of the nature of support (calcined or partially extracted), manifest the same selectivity to the unsaturated alcohol. The main values are in the range 5–10% for a conversion range of 20–90%. Accordingly, it can be claimed that the chemical nature of the active sites is similar for both samples, the main difference between these two materials consisting in different dispersion degrees (as already shown by the physicochemical characterization discussed above). For the samples prepared by precipitation methods, the nature of the active sites is significantly modified, since improved selectivity in CNOL is obtained. Consequently, modifications in the adsorption of cinnamaldehyde are assumed to be responsible for the improved selectivity. This statement is supported by the catalytic behavior of the IWI-MD/ER sample, whose dispersion is higher than for the samples prepared by precipitation, but whose selectivity to CNOL is low. It is obvious that the C=O bond is more easily activated on the catalytic sites generated from (phyllo)silicate-like phases as metallic precursors. It is worth recalling that the major advantage of this reaction consists of its high sensitivity to the electronic and geometric properties of the NPs supported on a catalytic support [84,86]. The surface structure of NPs is significantly changed in the 1–5 nm size range, since the number of corner, edge, and terrace atoms changes, affecting the surface electronic properties and thus the adsorption properties of the reactant molecule [4]. Additionally, the chemical nature of the support is also an important parameter for the adsorption of the reactant molecule [87]. Taking into account these two hypotheses, and on the basis of the TPR and XPS showing that part of the metallic precursors are not reduced at this temperature, it can be assumed that the unreduced phases are electron-deficient and thus affect the route of adsorption of CNA. The intimate contact between the surface metallic active sites and these electron-deficient sites is expected to promote the dissociation of hydrogen on the metallic sites, in parallel with the coordination of the oxygen of C=O bond on the neighboring electron-deficient site. As a result, this bond is polarized and finally hydrogenated to produce the unsaturated alcohol.

The possible presence of Cu^+ species, generated by the reduction of a residual Cu-PS-like phase (over precipitation-derived materials, as stated on TPR section), can also act positively on the selectivity. Indeed, it was previously reported that the presence of Cu^+ , in strong interaction with an alumina surface, could explain enhanced selectivity to CNOL [85].

3.4.2. Oxidation of CO

Monocomponent CuO and NiO supported on SBA-15 and prepared by the IWI-MD method were used as reference materials to stress the catalytic performance of the bicomponent copper–nickel phases. The conversion curves are depicted in Fig. 10.

When monometallic nickel is used as a catalyst, the activity, expressed as CO conversion, is practically zero irrespective of the reaction temperature. This behavior confirms some references showing that nickel oxide does not seem to exhibit good performance in CO oxidation [88] but disaffirms others that report nickel as a reactive metal oxide catalyst for CO oxidation by O_2 [89]. A

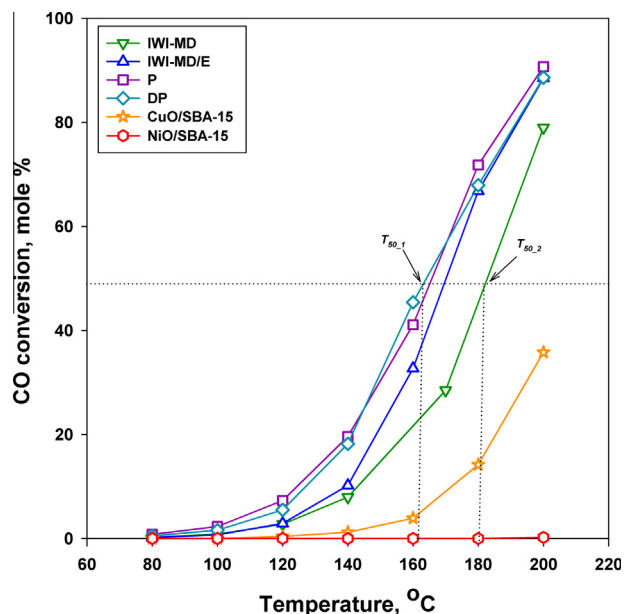


Fig. 10. CO conversion vs. reaction temperature for $\text{Cu}_4\text{Ni}_1/\text{SBA-15}$ after reduction–oxidation cycle. Test conditions: 100 mg of the catalyst activated under H_2 (15 mL min^{-1}) for 2 h at 350°C and then air (15 mL min^{-1}) at 350°C for 1 h. Reaction flow: 1:1 vol.% of CO and O_2 .

possible explanation for the results reported in Fig. 10 could be the oxidation state of Ni after the reduction–oxidation processes performed at 350°C before the catalytic test. The metallic nickel generated during the reduction step did not reoxidize to NiO during the reoxidation step, and thus the material manifests no activity for CO oxidation. Additionally, the calcination temperature (500°C) of the solid after impregnation and drying could also be an explanation for this poor activity, taking into account previous studies that assigned the low activity of monometallic nickel to the high calcination temperature, $>350^\circ\text{C}$ [90]. For $\text{CuO}/\text{SBA-15}$ catalyst, a CO conversion of 35% is reached at 200°C (Fig. 10). It was reported that the activity of copper catalysts in CO oxidation depends on the support, oxidation atmosphere, and preparation method [91]. Copper NPs (30–40 nm) supported on Al_2O_3 surface and molecular sieve-type supports present activity in CO oxidation at temperatures above 200°C for oxygen-lean conditions (2.6% O_2 and 3.8% CO), while under oxygen-rich conditions (28.6% O_2 and 3.8% CO), 50% CO conversion was reached at temperatures as low as 150°C . The use of rare-earth metals (e.g., cerium) as activators, dispersants, and stabilizers was also a strategy to enhance the catalytic activity of the copper-based active phase.

When CO and O_2 were in almost equal volume proportions (4.0% O_2 and 4.6% CO), the activity of copper supported on Al_2O_3 was much improved in comparison with that of $\text{Pd}/\text{Al}_2\text{O}_3$. However, these copper-based catalysts were active for temperatures above 160°C [91]. Likewise, Cao et al. [92] investigated CuO supported on meso–macroporous titania for CO oxidation and they established that the nature of the support, the metal oxide loading, the particle size, and the precalcination temperature are crucial for the catalytic performance of the resulted materials. However, a SMSI effect between copper and titania support also has to be taken into consideration for their studies, knowing that for these kinds of support (titania, ceria, vanadia), the affinity for the C–O bond is much stronger due to their oxygen surface deficiency in comparison to silica and alumina. In light of these reports, and also considering the satisfying tolerance to SO_2 of the supported CuO [88], a CO conversion of 35% at 200°C over CuO supported on SBA-15 silica could indicate that this material is a good catalyst for low-temperature oxidation reactions.

For the bimetallic $\text{Cu}_4\text{Ni}_1/\text{SBA-15}$ catalyst prepared by IWI-MD/C, a significant increase in catalytic activity, shown by a shift of the conversion curve toward the lower temperatures, is noticed ($T_{50,2} = 180^\circ\text{C}$). This sample shows a CO conversion of 50% at 180°C (T_{50}), which is three times higher than the conversion measured for $\text{CuO}/\text{SBA-15}$ (14.2%). A similar promotion effect was also observed over Au–Cu bimetallic phases [93], NiO–CuO bulk systems (equimolar transition metal oxide contents [89]), and nickel–copper supported on cordierite- $\text{Mg}_2\text{Al}_4\text{Si}_5\text{O}_{18}$ with 10–20 wt.% of each oxide [90]. For Au–Cu based catalysts the higher activity was explained by a synergistic effect between gold and copper, while for the copper–nickel systems, the improved activity was mainly attributed to the formation of an NiCuO_2 phase. Usually, the synergistic effect can be the result of an electron transfer from a component to another. Indeed, TPR and XPS results have shown such an interaction between nickel and copper for this sample based on the promoting effect of the electron transfer from nickel to copper, resulting in the increase of the surface electron density of copper. Thus, the adsorption of CO is more favorable on these sites as a result of the activation of the C–O bond. As shown by TPR and XPS, the strength of such metal–metal interactions is higher for the sample prepared by IWI-MD on the partially extracted support, which should undergo additional improved activity for CO oxidation. Accordingly, the CO conversion curve shows $T_{50,1} = 170^\circ\text{C}$ for this sample, and thus a temperature 10°C lower than for the sample prepared on the calcined support. For the samples prepared by precipitation methods, additional improvement in the CO conversion can be noticed, 50% CO conversion being observed at 160°C ($T_{50,1} = 160^\circ\text{C}$). For these two samples, the higher activity is explained in a manner similar to that for the selectivity to CNOL, i.e., by the existence of the surface electron-deficient sites with improved affinity for the C–O bond.

4. Conclusions

Copper–nickel metal (oxide) NPs (5 wt.% metal, and Cu:Ni weight ratio 4:1) were prepared by loading the corresponding precursors on the SBA-15 silica surface by IWI-MD, P, and DP approaches. For IWI-MD, calcined and partially extracted SBA-15 were used as supports. The use of SBA-15 occluded with P123 template was evidenced to be a good strategy to obtain highly dispersed copper-rich copper–nickel based NPs on the internal surface of SBA-15. The degree of dispersion, using this approach, is higher than that obtained for NPs prepared by precipitation (either with Na_2CO_3 or urea), while the textural properties of the sample did not suffer from any change. Moreover, according to in situ XRD after thermoprogrammed reduction, the copper–nickel NPs manifest improved thermostability in comparison with NPs prepared by precipitation.

Additionally, different metal–metal and metal–support interactions were noticed depending on the preparation method, bicomponent NPs prepared by IWI-MD being mainly characterized by metal–metal interactions, while for those prepared by precipitation, the metal–support interactions were more evident. The supported metal (oxide) NPs were used for the hydrogenation of cinnamaldehyde and CO oxidation reactions. For the cinnamaldehyde hydrogenation, the highest activity (conversion of 100% in 120 min of reaction) was measured for the samples prepared by impregnation on the partially extracted SBA-15 and by precipitation with urea. The improved activities are associated with the high dispersion of the metallic active phases in these materials. Enhanced selectivity to unsaturated alcohol was noticed for the samples prepared by precipitation and related to the formation of dual-metal electron-deficient sites. For CO oxidation, the samples prepared by precipitation were more active than the samples

prepared by impregnation, also because of these electron-deficient sites with high affinity with the C–O bond.

Acknowledgments

This work was partially supported by two grants of the Romanian National Authority for Scientific Research, CNCS-UEFISCDI (Projects PN-II-RU-TE-2012-3-0403 and PN-II-ID-PCE-2011-3-0868).

Appendix A. Supplementary material

Supplementary data associated with this article can be found, in the online version, at <http://dx.doi.org/10.1016/j.jcat.2016.04.004>.

TG-DSC curves of as-made and partially extracted SBA-15 support; TEM images collected at different magnifications besides EDX spectra collected in different areas the for P/C sample; and XPS spectra for all four samples are available free of charge via the Internet.

References

- [1] A.H. Faraji, P. Wipf, *Bioorg. Med. Chem.* 17 (2009) 2950.
- [2] A. Cao, C. Vesper, *Nat. Mater.* 9 (2010) 75.
- [3] L. Starkey Ott, R.G. Finke, *Coord. Chem. Rev.* 251 (2007) 1075.
- [4] R.M. Rioux, H. Songa, M. Grass, S. Habas, K. Niesz, J.D. Hoefelmeyer, P. Yang, G. A. Somorjai, *Top. Catal.* 39 (2006) 167.
- [5] J.G. Speight, B. Ozum, *Petroleum Refining Processes*, Marcel Dekker, New York, 2002, pp. 294.
- [6] S.H. Joo, J.Y. Park, C.-K. Tsung, Y. Yamada, P. Yang, G.A. Somorjai, *Nat. Mater.* 8 (2009) 126.
- [7] D. Astruc, in: D. Astruc (Ed.), *Nanoparticles and Catalysis*, vol. 1, Wiley-VCH Verlag GmbH & Co. KGaA, Weinheim, 2008, pp. 24.
- [8] C.N. Satterfield, *Heterogeneous Catalysis in Industrial Practice*, second ed., Krieger Publishing Company, Malabar, Florida, 1991, pp. 112.
- [9] V. La Parola, B. Dragoi, A. Ungureanu, E. Dumitriu, A.M. Venezia, *Appl. Catal., A* 386 (2010) 43.
- [10] C.S. Chen, Y.T. Lai, T.W. Lai, J.H. Wu, C.H. Chen, J.F. Lee, H.M. Kao, *ACS Catal.* 3 (2013) 667.
- [11] R.P. Jumde, C. Evangelisti, A. Mandoli, N. Scotti, R. Psaro, *J. Catal.* 324 (2015) 25.
- [12] A. Ungureanu, B. Dragoi, A. Chiriac, C. Ciotonea, S. Royer, D. Duprez, A.S. Mamede, E. Dumitriu, *ACS Appl. Mater. Interfaces* 5 (2013) 3010.
- [13] B. Dragoi, A. Ungureanu, A. Chiriac, V. Hulea, S. Royer, E. Dumitriu, *Catal. Sci. Technol.* 3 (2013) 2319.
- [14] C. Papadopolou, H. Matralis, X. Verykios, in: L. Guzzi, A. Erdöhelyi (Eds.), *Catalysis for Alternative Energy Generation*, Springer, New York, 2012, pp. 112.
- [15] D. Zhao, J. Feng, Q. Huo, N. Melosh, G.H. Fredrickson, B.F. Chmelka, G.D. Stucky, *Science* 279 (1998) 548.
- [16] G.J. de A.A. Soler-Illia, E.L. Crepaldi, D. Grosso, C. Sanchez, *Curr. Opin. Colloid Interface Sci.* 8 (2003) 109.
- [17] C.-M. Yang, B. Zibrowius, W. Schmidt, F. Schuth, *Chem. Mater.* 15 (2003) 3739.
- [18] S.H. Joo, R. Ryoo, M. Kruk, M. Jaroniec, *J. Phys. Chem. B* 106 (2002) 4640.
- [19] J. Sun, D. Ma, H. Zhang, X. Liu, X. Han, X. Bao, G. Weinberg, N. Pfänder, D. Su, *J. Am. Chem. Soc.* 128 (2006) 15756.
- [20] Z.-J. Wang, X. Yongbing, L. Chang-Jun, *J. Phys. Chem. C* 112 (2008) 19818.
- [21] J. Zhu, W. Tao, X. Xuellian, X. Ping, L. Jinlin, *Appl. Catal., B* 130–131 (2013) 197.
- [22] P. Munnik, M. Wolters, A. Gabriësson, S.D. Pollington, G. Headdock, J.H. Bitter, P.E. de Jongh, K.P. de Jong, *J. Phys. Chem. C* 115 (2011) 14698.
- [23] T. Tsoncheva, V. Dal Santo, A. Gallo, N. Scotti, M. Dimitrov, D. Kovacheva, *Appl. Catal., A* 406 (2011) 13.
- [24] L.-F. Chen, P.-J. Guo, L.-J. Zhu, M.-H. Qiao, W. Shen, H.-L. Xu, K.-N. Fan, *Appl. Catal., A* 356 (2009) 129.
- [25] F. Boubekr, A. Davidson, S. Casale, P. Massiani, *Microporous Mesoporous Mater.* 141 (2011) 157.
- [26] J. Taghavimoghaddam, G.P. Knowles, A.L. Chaffee, *J. Mol. Catal. A: Chem.* 358 (2012) 79.
- [27] H. Friedrich, J.R.A. Sietsma, P.E. de Jongh, A.J. Verkleij, K.P. de Jong, *J. Am. Chem. Soc.* 129 (2007) 10249.
- [28] A. Rumpelcker, F. Kleitz, E.-L. Salabas, F. Schuth, *Chem. Mater.* 19 (2007) 485.
- [29] W. Yue, W. Zhou, *Chem. Mater.* 19 (2007) 2359.
- [30] M.A. Wahab, F. Darain, *Nanotechnology* 25 (2014) 165701.
- [31] A.-H. Lu, D. Zhao, Y. Wan (Eds.), *Nanocasting, A Versatile Strategy for Creating Nanostructured Porous Materials*, RSC Publishing, Cambridge, UK, 2010, pp. 1.
- [32] C.M. Yang, H.A. Lin, B. Zibrowius, B. Spliethoff, F. Schuth, S.C. Liou, M.W. Chu, C. H. Chen, *Chem. Mater.* 19 (2007) 3205.
- [33] S. Valange, R. Palacio, A. Charnot, J. Barrault, A. Louati, Z. Gabelica, *J. Mol. Catal. A: Chem.* 305 (2009) 24.
- [34] X. Zhong, J. Barbier Jr., D. Duprez, H. Zhang, S. Royer, *Appl. Catal., B* 121 (2012) 123.
- [35] I. Yuranov, P. Moeckli, E. Suvorova, P. Buffat, L. Kiwi-Minsker, A. Renken, *J. Mol. Catal. A: Chem.* 192 (2003) 239.
- [36] Q. Jiang, Z.Y. Wu, Y.M. Wang, Y. Cao, C.F. Zhou, J.H. Zhu, *J. Mater. Chem.* 16 (2006) 1536.
- [37] W.-H. Tian, L.-B. Sun, X.-L. Song, X.-Q. Liu, Y. Yinand, G.-S. He, *Langmuir* 26 (2010) 17398.
- [38] Y. Yin, D.-M. Xue, X.-Q. Liu, G. Xu, P. Ye, M.-Y. Wu, L.-B. Sun, *Chem. Commun.* 48 (2012) 9495.
- [39] A. Lekhal, J. Benjamin Glasser, G. Johannes Khinast, in: J.R. Regalbuto (Ed.), *Catalyst Preparation, Science and Engineering*, CRC Press, Taylor & Francis Group, 2007, pp. 379.
- [40] A. Ungureanu, B. Dragoi, A. Chiriac, S. Royer, D. Duprez, E. Dumitriu, *J. Mater. Chem.* 21 (2011) 12529.
- [41] B.R. Cuenya, *Thin Solid Films* 518 (2010) 3127.
- [42] R. Ferrando, J. Jellinek, R.L. Johnston, *Chem. Rev.* 108 (2008) 845.
- [43] K.P. de Jong, in: K.P. de Jong (Ed.), *Synthesis of Solid Catalysts*, Wiley-VCH Verlag GmbH & Co. KGaA, Weinheim, 2009, pp. 111.
- [44] C. Louis, in: J.R. Regalbuto (Ed.), *Catalyst Preparation, Science and Engineering*, CRC Press, Taylor & Francis Group, 2007, pp. 319.
- [45] M. Lok, in: K.P. de Jong (Ed.), *Synthesis of Solid Catalysts*, Wiley-VCH Verlag GmbH & Co. KGaA, Weinheim, 2009, pp. 135.
- [46] C. Ciotonea, B. Dragoi, A. Ungureanu, A. Chiriac, S. Petit, S. Royer, E. Dumitriu, *Chem. Commun.* 49 (2013) 7665.
- [47] H. Liu, H. Wang, J. Shen, Y. Sun, Z. Liu, *Appl. Catal., A* 337 (2008) 138.
- [48] S.F.H. Tasfy, N.A.M. Zabidi, D. Subbarao, *J. Appl. Sci.* 11 (2011) 1150.
- [49] Q. Wu, W.L. Eriksen, L.D.L. Duchstein, J.M. Christensen, C.D. Damsgaard, J.B. Wagner, B. Temel, J.-D. Grunwaldt, A.D. Jensen, *Catal. Sci. Technol.* 4 (2014) 378.
- [50] S. Wang, W. Guo, H. Wang, L. Zhu, S. Yin, K. Qiu, *New J. Chem.* 38 (2014) 2792.
- [51] P. Munnik, P.E. de Jongh, K.P. de Jong, *Chem. Rev.* 115 (2015) 6687.
- [52] H.-A. Lin, C.-H. Liu, W.-C. Huang, S.-C. Liou, M.-W. Chu, C.-H. Chen, J.-F. Lee, C.-M. Yang, *Chem. Mater.* 20 (2008) 6617.
- [53] C.H. Liu, Y. Guan, E.J.M. Hensen, J.F. Lee, C.M. Yang, *J. Catal.* 282 (2011) 94.
- [54] C.H. Liu, N.C. Lai, S.C. Liou, M.W. Chu, C.H. Chen, C.M. Yang, *Microporous Mesoporous Mater.* 179 (2013) 40.
- [55] E. Besson, A. Mehdi, C. Reye, R.J.P. Corriu, *J. Mater. Chem.* 19 (2009) 4746.
- [56] C. Setzer, G. van Essche, N. Pryor, in: F. Schüth, K. Sing, J. Weitkamp (Eds.), *Handbook of Porous Solids*, vol. 1, Springer, Weinheim, 2002, p. 1551.
- [57] W. Lifeng, R.T. Yang, *J. Phys. Chem. C* 115 (2011) 21264.
- [58] A. Galarneau, H. Cambon, F. Di Renzo, F. Fajula, *Langmuir* 17 (2001) 8328.
- [59] J.R.A. Sietsma, J.D. Meeldijk, M. Versluijs-Helder, A. Broersma, A.J. van Dillen, P. E. de Jongh, K.P. de Jong, *Chem. Mater.* 20 (2008) 2921.
- [60] A. Carrero, J.A. Calles, A.J. Vizcaino, *Appl. Catal., A* 327 (2007) 82.
- [61] G. Aguilu, F. Gracia, P. Araya, *Appl. Catal., A* 343 (2008) 16.
- [62] S.M. Cioclitu, M. Salou, Y. Kiyozumi, S.-I. Niwa, F. Mizukamia, M. Haneda, *J. Mater. Chem.* 13 (2003) 602.
- [63] R. Brown, M.E. Cooper, D.A. Whan, *Appl. Catal.* 3 (1982) 177.
- [64] S. Zhu, X. Gao, Y. Zhu, W. Fan, J. Wang, Y. Li, *Catal. Sci. Technol.* 5 (2015) 1169.
- [65] X.C. Zheng, S.H. Wu, S.P. Wang, S.R. Wang, S.M. Zhang, W.P. Huang, *Appl. Catal., A* 283 (2005) 217.
- [66] Z. Liu, M.D. Amiridis, Y. Chen, *J. Phys. Chem. B* 109 (2005) 1251.
- [67] C.-H. Tu, A.-Q. Wang, M.-Y. Zheng, X.-D. Wang, T. Zhang, *Appl. Catal., A* 297 (2006) 40.
- [68] P.C.M. van Stiphout, D.E. Stobbe, F.T.V.D. Scheur, J.W. Geus, *Appl. Catal.* 40 (1988) 219.
- [69] A. Gervasini, M. Manzoli, G. Martra, A. Ponti, N. Ravasio, L. Sordelli, F. Zaccheria, *J. Phys. Chem. B* 110 (2006) 7851.
- [70] A.R. Naghsh, T.H. Etsell, S. Xu, *Chem. Mater.* 18 (2006) 2480.
- [71] J.C. Vedrine, G. Hollinger, T.M. Duc, *J. Phys. Chem.* 82 (1978) 1515.
- [72] T. Lehmann, T. Wolff, C. Hamel, P. Veit, B. Garke, A. Seidel-Morgenstern, *Microporous Mesoporous Mater.* 151 (2012) 113.
- [73] M.-J. Suh, S.-K. Ihm, *Top. Catal.* 53 (2010) 447.
- [74] L. Xiaowei, S. Mingmin, H. Xi, Z. Haiyang, G. Fei, K. Yan, D. Lin, C. Yi, *J. Phys. Chem. B* 109 (2005) 3949.
- [75] H. Zhu, Y. Wu, X. Zhao, H. Wan, L. Yang, J. Hong, Q. Yu, L. Dong, Y. Chen, C. Jian, J. Wei, P. Xu, *J. Mol. Catal. A: Chem.* 243 (2006) 24.
- [76] A. Kaddouri, N. Dupont, P. Gelin, P. Delichere, *Catal. Lett.* 141 (2011) 1581.
- [77] K. Yoshida, C. Gonzalez-Arellano, R. Luque, P.L. Gai, *Appl. Catal., A* 379 (2010) 38.
- [78] I. Nakai, Y. Sugitani, K. Nagashima, Y. Niwa, *J. Inorg. Nucl. Chem.* 40 (1978) 789.
- [79] P. Burattin, M. Che, C. Louis, *J. Phys. Chem. B* 102 (1998) 2722.
- [80] P. Burattin, M. Che, C. Louis, *J. Phys. Chem. B* 103 (1999) 6171.
- [81] C.J.G. van der Grift, P.A. Elberse, A. Mulder, J.W. Geus, *Appl. Catal., A* 59 (1990) 275.
- [82] C. Svatopluk, W.R. Glomm, E.A. Blekkan, *Catal. Today* 147 (2009) 217.
- [83] A. Yin, C. Wen, X. Guo, W.L. Dai, K. Fan, *J. Catal.* 280 (2011) 77.
- [84] P. Maki-Arvela, J. Hajek, T. Salmi, D.Y. Murzin, *Appl. Catal., A* 292 (2005) 1.
- [85] S. Valange, A. Derouault, J. Barrault, Z. Gabelica, *J. Mol. Catal. A: Chem.* 228 (2005) 255.
- [86] Y. Yuan, S. Yao, M. Wang, S. Lou, N. Yan, *Curr. Org. Chem.* 17 (2013) 400.
- [87] K.J.A. Raj, M.G. Prakash, T. Elangovan, B. Viswanathan, *Catal. Lett.* 142 (2012) 87.
- [88] S. Royer, D. Duprez, *ChemCatChem* 3 (2011) 24.
- [89] H.G. El-Shobaky, *Appl. Catal., A* 278 (2004) 1.
- [90] H.G. El-Shobaky, Y.M. Fahmy, *Appl. Catal., B* 63 (2006) 168.
- [91] F.-L. Du, Z.-L. Cui, Z.-K. Zhang, S.-Y. Chem, *J. Nat. Gas Chem.* 6 (1997) 135.
- [92] J.-L. Cao, G.-S. Shao, T.-Y. Ma, Y. Wang, T.-Z. Ren, S.-H. Wu, Z.-Y. Yuan, *J. Mater. Sci.* 44 (2009) 6717.
- [93] X. Liu, A. Wang, L. Li, T. Zhang, C.-Y. Mou, J.-F. Lee, *J. Catal.* 278 (2011) 288.